Contents lists available at ScienceDirect

Solid-State Electronics

journal homepage: www.elsevier.com/locate/sse

SOLID-STATE
ELECTRONICS
An International Journal

Modeling and simulation of low power ferroelectric non-volatile memory tunnel field effect transistors using silicon-doped hafnium oxide as gate dielectric ☆

CrossMark

A. Saeidi *, A. Biswas, Adrian M. Ionescu

Laboratory of Micro and Nano-electronic Devices, Ecole Polytechnique Fédérale de Lausanne, Lausanne, Switzerland

ARTICLE INFO

ABSTRACT

The implementation and operation of the nonvolatile ferroelectric memory (NVM) tunnel field effect transistors with silicon-doped HfO$_2$ is proposed and theoretically examined for the first time, showing that ferroelectric nonvolatile tunnel field effect transistor (Fe-TFET) can operate as ultra-low power non-volatile memory even in aggressively scaled dimensions. A Fe-TFET analytical model is derived by combining the pseudo 2-D Poisson equation and Maxwell's equation. The model describes the Fe-TFET behavior when a time-dependent voltage is applied to the device with hysteretic output characteristic due to the ferroelectric's dipole switching. The theoretical results provide unique insights into how device geometry and ferroelectric properties affect the Fe-TFET transfer characteristic. The recently explored ferroelectric, silicon-doped HfO$_2$ is employed as the gate ferroelectric. With the ability to engineer ferroelectricity in HfO$_2$ thin films, a high-K dielectric well established in memory devices, the silicon-doped HfO$_2$ opens a new route for improved manufacturability and scalability of future 1-T ferroelectric memories. In the current research, a Si:HfO$_2$ based Fe-TFET with large memory window and low power dissipation is designed and simulated. Utilizing our presented model, the device characteristics of a Fe-TFET that takes full benefits from Si:HfO$_2$ is compared with the same devices using well-known perovskite ferroelectrics. Finally, the Fe-TFET is compared with a conventional ferroelectric memory transistor highlighting the advantages of using tunneling memory devices.

© 2016 Elsevier Ltd. All rights reserved.

1. Introduction

Ferroelectric materials can be utilized as electrically switchable nonvolatile data storage elements as their polarization can change by applying an external electric field. Recently, novel devices called ferroelectric TFETs [1], and ferroelectric FETs have been proposed as promising candidates for future nonvolatile memory applications [2,3]. In ferroelectric field effect devices, two stable states of the ferroelectric's polarization are used for data storage [4]. Nonvolatile data storage, fast writing, and nondestructive read-out operation have been reported for ferroelectric field effect transistors [5]. However, the industrial implementation of ferroelectric devices especially in nanoscale still missing due to the integration and scaling obstacles of conventionally used perovskite type ferroelectrics such as Lead Zirconate Titanate (PZT). The recently discovered ferroelectricity in HfO$_2$ thin films [6], enabled CMOS-compatible

manufacturing of highly scaled ferroelectric devices down to 28 nm ground rule [6,7].

By scaling devices down to the nanoscale, power density becomes a challenging issue as the power density per area of the chip increases. The tunneling field effect transistors have been investigated intensely in recent years [8] due to their considerable potentials for ultra-low power applications [9,10]. Using the advantages of both ferroelectric thin films for data storage and TFETs as energy efficient devices, it is possible to design a new class of nonvolatile memories, with a relatively large memory window, fast writing, nondestructive read-out operation, and low power consumption. In this work, we propose a comprehensive, quantitative model for investigation of Fe-TFETs. The successful design of a Fe-TFET for nonvolatile data storage requires a thorough understanding of the device operation principals. It is necessary to develop an analytical model for Fe-TFETs design optimization. Hence, an analytical model for Fe-TFETs is proposed and verified with Sentaurus TCAD [11] simulation tool. The model is developed by solving the 2-D Poisson equation [12] for a single gate TFET and considering the effect of the ferroelectric polarization on the sur-

---

face potential. The polarization effect is calculated by solving Maxwell's first equation in the gate stack. A numerical method is employed to calculate the polarization hysteresis for both saturated and nonsaturated hysteresis loops [13]. Based on our proposed model, memory window of the ferroelectric memory TFETs using different ferroelectric materials is investigated. It should be noted that short channel effects are neglected in the proposed model, and a 200 nm gate length device is utilized for model verification. Finally, a 28 nm gate length Fe-TFET benefits from Si:HfO$_2$ as the gate ferroelectric is designed and simulated using Sentaurus TCAD commercial simulator. Results confirm that the proposed device can be employed as the future of nonvolatile memories. Moreover, we present that the ferroelectrics negative capacitance improves the device's output current by boosting the gate potential.

2. Device modeling

2.1. Approach and definitions

In this paper, an n-type SOI ferroelectric TFET is studied. The device is schematically depicted in Fig. 1. The length of the channel is 200 nm to suppress short channel effects, the doping concentration of the lightly doped channel is 5×10^{14} cm^{-3}, the highly doped $p+$ source concentration is 1×10^{20} cm^{-3} and the $n+$ doped drain is 1×10^{18} cm^{-3} to eliminate the ambipolar behavior [13]. The silicon-doped HfO$_2$ is utilized as ferroelectric layer due to its unique property of exhibiting the ferroelectricity even in a 5 nm thick, thin film [14,15]. For the model verification, we have used 10 nm of Si:HfO$_2$ with 9 μC/cm^2 remanent polarization and 1.1 mV/cm coercive field [6]. We will discuss how the relatively high coercive field and remanent polarization guarantee a large memory window (and retention time) in the Ferroelectric Memory TFET.

To develop the ferroelectric TFET model, we have combined the switching analytical modeling of ferroelectric capacitors [16] with the Band-to-Band Tunneling modeling of TFETs. Wu et al. [12] proposed the analytical modeling of TFETs based on the gate and drain dual modulation effects by solving Poisson equation in the device channel. Miller et al. [17,13,18] developed the compact modeling of ferroelectric capacitors that accurately describes the dipole polarization switching by employing Maxwell's first equation. We employed Maxwell and Poisson equations consistently to precisely calculate the surface potential profile along the channel. Finally, the device current is calculated by determining the potential profile around the tunneling junctions. The computer aided design (TCAD) tool Sentaurus is used to verify the proposed model. The non-local band-to-band tunneling (BTBT) model is enabled to account tunneling mechanism [19]. In order to calculate the

tunneling probability using the electron-hole wave vector throughout the tunneling path, the non-local model uses Wetzel-Kramer-Brillouin (WKB) approximation. Also, Fermi statistics and Shockley-Reed-Hall (SRH) recombinations are adopted while the gate tunneling is ignored. In order to incorporate the ferroelectric properties of the gate stack, we have enabled Ferro model in our simulations. Moreover, the standard library of Sentaurus TCAD is used for linear dielectrics (where the SiO$_2$ and Si$_3$N$_4$ relative permittivity is 3.9 and 7.5 respectively). These models are considered in all TCAD simulations unless otherwise mentioned. It should be noted that the ferroelectric layer is considered ideal from the point of view of hysteresis loss related issues like fatigue (loss of switched charge owing to repetitive destructive reads), retention (decreasing the stored charge to a level where the positive and negative state of the polarization cannot be reliably sensed), and direct current breakdown (as a result of applying constant writing voltage) have been neglected [20].

2.2. Model

In this subsection, we describe the relation between the ferroelectric polarization and the silicon surface potential in a metal-ferroelectric-oxide-semiconductor structure [21]. The electrostatic equations are derived starting with Maxwell's equation,

$$\nabla \cdot D = \rho, \tag{1}$$

$$D = \epsilon_0 \epsilon E + P_d, \tag{2}$$

where D is the displacement, ρ is the free charge density, E is the electrical field, ϵ_0 is the vacuum permittivity, ϵ is the linear dielectric constant, and P_d is the contribution of the switching dipoles. Solving (1) and (2) in conjunction with the definition $E = -\nabla \phi$ (ϕ is the electrostatic potential) leads us to:

$$V_{GB} = \phi_s - \frac{\sigma_s}{C_{stack}} - P_d(E_f) \frac{d_f}{\epsilon_0 \epsilon_f}. \tag{3}$$

In (3), C_{stack} describes the gate total capacitance, σ_s is the silicon charge, d_f and ϵ_f are ferroelectric thickness and relative permittivity and ϕ_s is the silicon surface potential. The ferroelectric polarization changes the surface potential by a value of $P_d(d_f/\epsilon_0 \epsilon_f)$. The ferroelectric polarization can also be calculated using Landau-Khalatnikov (LK) theory [22–24]. Using Landau theory, (3) can be rewritten as follow:

$$V_{GB} - \phi_s + \frac{\sigma_s}{C_{Buffer}} = (2\alpha t_f)P_d(E_f) + (4\beta t_f)P_d^3(E_f) + (6\gamma t_f)P_d^5(E_f), \tag{4}$$

where $\alpha, \beta,$ and γ are the ferroelectric Landau parameters, t_f is the ferroelectric thickness, and C_{Buffer} is the capacitance of the buffer layer. The Fe-TFET modeling can be obtained using either (3) or (4). However, (3) is employed in this study to derive a simple analytical model for the device operation.

We explain the Fe-TFET behavior by considering the effect of the polarization on the surface potential for a known polarization. Combining Maxwell's first equation with Wu's analytical solution for TFET surface potential [12], the surface potential in middle of the channel for the whole range of the operation can be given as

$$\phi_{ch} = F + \frac{kT}{q} \ln \left\{ \frac{q}{kT} \left[\frac{kT}{q} + \frac{\sqrt{F}}{\sqrt{F}+\gamma} \left(V_{GS} - V_{fb} + P_d \frac{d_f}{\epsilon_0 \epsilon_f} - F \right) \right. \right.$$
$$\left. \left. + \frac{1}{2} \left[\frac{F}{(\sqrt{F}+\gamma)^2} - \frac{\gamma[F-2]}{2(\sqrt{F}+\gamma)^3} \right] \left(V_{GS} - V_{fb} + P_d \frac{d_f}{\epsilon_0 \epsilon_f} - F \right)^2 \right] \right\}, \tag{5}$$

$$F = \frac{1}{2} \left\{ V_{DS} + \Phi + \phi_{ch,dep} - \sqrt{(\phi_{ch,dep} - V_{DS} - \Phi)^2 + \delta^2} \right\}, \tag{6}$$
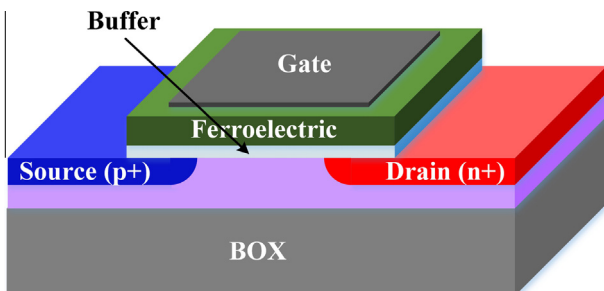

Fig. 1. The device schematic of an SOI Fe-TFET where the gate stack of a conventional single gate TFET is replaced with a series combinations of a ferroelectric and a linear dielectric.

$$\phi_{ch,dep} = \left\{ \sqrt{V_{GS} - V_{fb} + P_d \frac{d_f}{\epsilon_0 \epsilon_f} + \frac{\gamma^2}{4}} - \frac{\gamma}{2} \right\}^2, \tag{7}$$

where V_{fb} is the flat band voltage, T is the temperature, k is the Boltzmann's constant, q is the electrical charge of a single electron, γ is the body factor defines as $\sqrt{2\epsilon_{si}qN_{ch}}/C_{stack}$ (N_{ch} is the channel doping), δ is a small smoothing factor and $\phi_{ch,dep}$ is the surface potential in the gate control regime [12]. Φ is the required surface potential for sufficient inversion charge to screen the gate modulation and can be expressed as $(kT/q) \ln (N_{ch}N_{inv}/n_i^2)$, and N_{inv} is the required inversion charge density to screen the gate voltage.

An accurate expression of the surface potential profile around the tunnel junction is needed to calculate the tunneling current. We use the pseudo 2-D Poisson equation to obtain the potential profile along the channel [25]. The parabolic approximation of the potential in a direction normal to the surface is adopted so that the Poisson equation can be reduced to the well-known form

$$\frac{d^2 \phi_s(x)}{dx^2} - \frac{\phi_s(x) - \left(V_{GS} - V_{fb} + P_d \frac{d_f}{\epsilon_0 \epsilon_f}\right)}{\lambda^2} = \frac{qN_{ch}}{\epsilon_{si}}, \tag{8}$$

where $\lambda = \sqrt{\epsilon_{si}t_{si}/C_{stack}}$ (t_{si} and ϵ_{si} represent the silicon thickness and relative permittivity) is the characteristic length of the channel [12]. Solving (8) by considering the boundary conditions and the continuity of potential and electric field at the source-channel and channel-drain junctions, the surface potential profile around tunneling junctions can be obtained as

$$\phi_s(x) = (V_{GS(eff)}) + (\phi_{ch} - V_{GS(eff)}) \cosh\left(\frac{x - x_{sc}}{\lambda}\right) \cdots 0 \leqslant x \leqslant x_{sc}, \tag{9}$$

$$\phi_s(x) = (V_{GS(eff)}) + (\phi_{ch} - V_{GS(eff)}) \cosh\left(\frac{x - x_{sd}}{\lambda}\right) \cdots x_{cd} \leqslant x \leqslant L_{ch}, \tag{10}$$

$$x_{sc} = \lambda \cosh\left(\frac{V_{S0} - (V_{GS(eff)})}{\phi_{ch} - (V_{GS(eff)})}\right), \tag{11}$$

$$x_{cd} = L_{ch} - \lambda \cdot \cosh^{-1}\left(\frac{V_{D(eff)} - (V_{GS(eff)})}{\phi_{ch} - (V_{GS(eff)})}\right). \tag{12}$$

In the performed equations, V_{S0} subscribes to the source potential, $V_{D(eff)}$ is the potential in the drain region $(V_{D(eff)} = V_{S0} + V_{bi,SD} + V_{DS})$, $V_{GS(eff)}$ is the gate effective voltage $(V_{GS(eff)} = V_{GS} - V_{fb} + P_d(d_f/\epsilon_0 \epsilon_f) - (qN_{ch}/\epsilon_{si})\lambda^2)$, and ϕ_{ch} is the surface potential in the center of the channel that we have derived before. The tunneling width at the source junction can be expressed as

$$W_{t,min} = x\left(V_{S0} + \frac{E_g}{q}\right) - x(V_{S0})$$
$$= x_{sc} - \lambda \cdot \cosh^{-1}\left(\frac{V_{D(eff)} - (V_{GS(eff)})}{\phi_{ch} - (V_{GS(eff)})}\right), \tag{13}$$

$$W_{t,max} = x(\phi_{ch}) - x\left(\phi_{ch} - \frac{E_g}{q}\right)$$
$$= \lambda \cosh^{-1}\left(\frac{V_{S0} + \frac{E_g}{q} - (V_{GS(eff)})}{\phi_{ch} - (V_{GS(eff)})}\right). \tag{14}$$

where $W_{t,min}$ and $W_{t,max}$ are the minimum and maximum of the tunneling width along the lateral tunneling path at the source-channel junction (the source-channel and channel-drain tunneling widthes are schematically depicted in Fig. 2). Regarding Kane's model [26], the tunneling current can be calculated by integrating the tunneling probability over the effective tunneling length,
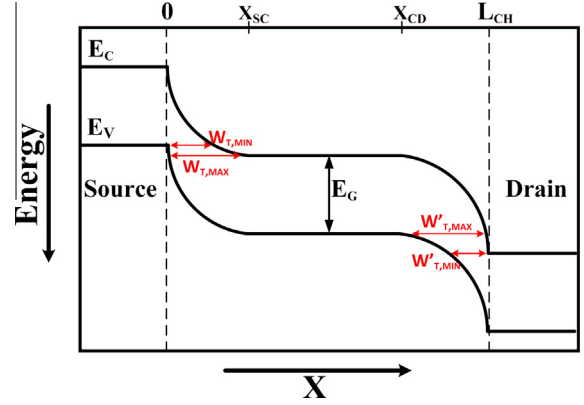

Fig. 2. The energy bands in a tunneling field effect transistor indicating the maximum and minimum of the tunneling width in the source-channel and channel-drain junctions [12]. X_{SC} and X_{CD} represent the source and drain tunneling junction width.

$$I_{tunnel,S \to C} = q.W. \int_{W_{t,min}}^{W_{t,max}} \int_0^{t_{si}} G_{Kane} dy dx. \tag{15}$$

In (15), G_{Kane} is the Kane's tunneling probability factor. The tunneling current at the drain junction can be calculated similarly,

$$W'_{t,min} = x(V_{D(eff)}) - x\left(V_{D(eff)} - \frac{E_g}{q}\right), \tag{16}$$

$$W'_{t,max} = x\left(\phi_{ch} + \frac{E_g}{q}\right) - x(\phi_{ch}). \tag{17}$$

$$I_{tunnel,C \to D} = q.W. \int_{W'_{t,min}}^{W'_{t,max}} \int_0^{t_{si}} G_{Kane} dy dx, \tag{18}$$

where $W'_{t,min}$ and $W'_{t,max}$ are minimum and maximum of the lateral path at the channel-drain junction. Finally, the total value of the device output current can be expressed as,

$$I_{DS} = I_{tunnel,S \to C} + I_{tunnel,C \to D}. \tag{19}$$

2.3. Dipole polarization

The value of the dipole polarization in each step is a function of the history of the applied electric field. Therefore, the polarization is determined by integrating $dP_d(E_f)/dE_f$ from a specified initial condition. Since this form has been extensively discussed before for the arbitrary field histories [17], the results are simply stated here. The saturated polarization hysteresis loop is defined by

$$P_{sat}^+(E_f) = P_s \tanh\left(\frac{E_f - E_c}{2\delta}\right), P_{sat}^- = -P_{sat}^+(-E), \tag{20}$$

where

$$\delta = E_c \left[\ln\left(\frac{1 + \frac{P_r}{P_s}}{1 - \frac{P_r}{P_s}}\right)\right]^{-1}, \tag{21}$$

and + (or −) superscript signifies the positive (or negative) going branch of the loop. The derivative of the polarization is given by the following equations:

$$\frac{dP_d}{dE_f} = \Gamma \frac{dP_{sat}}{dE_f}, \tag{22}$$

$$\Gamma = 1 - \tanh\left[\left(\frac{P_d - P_{sat}}{\xi P_s - P_d}\right)^{\frac{1}{2}}\right]. \tag{23}$$

where $\xi = +1$ when $dE/dt > 0$ and $\xi = -1$ when $dE/dt < 0$.

Considering (1)–(19), the Fe-TFET drain current can be calculated as a function of the gate voltage history, device geometry, and material properties while the dipole polarization can be obtained using (20)–(23). In the following section, we will present a numerical analysis technique in order to obtain the Fe-TFET transfer characteristic.

2.4. Numerical analysis technique

Since the ferroelectric polarization depends on the history of the electric field, the polarization can be obtained by integrating from a known value. For the first step, we should define the initial values for the gate voltage and the polarization. Note that the initial conditions must satisfy the physical requirement that the polarization lies on or within the hysteresis loop. We considered $V_g = V_{fb}$ and $P_d = 0$ as the initial condition. Having the polarization and the gate voltage, all TFET parameters are calculated using (1)–(19). Furthermore, the ferroelectric field and the silicon surface charge density can be calculated as follows:

$$\sigma_s = -\sqrt{2\epsilon_{si}kTN_{ch}}\left\{q\frac{\phi_{ch}}{kT} + \left(\frac{n_i}{N_{ch}}\right)^2 \exp\left(q\frac{\phi_{ch}-V}{kT}\right)\right\}^{\frac{1}{2}}, \quad (24)$$

$$E_f = -\frac{\sigma_s + P_d(f)}{\epsilon_0\epsilon_f}. \quad (25)$$

The approach to perform the integration from the initial conditions to a new set of conditions is to compute the m'th value of the relevant quantities, and numerically integrate. We now introduce subscript m, which signifies that the given quantity is evaluated at the m'th integration increment. First, we should solve Eqs. (1)–(19) to find the m'th value of the surface potential. Then, we calculate the m'th value of the silicon surface charge and the electric field inside the ferroelectric film using Eqs. (24) and (25). The polarization can be expressed as

$$P_d(E_{m+1}) = P_d(E_m) + (E_{m+1} - E_m)\frac{d}{dE}[P_d(E)]_{E_m}. \quad (26)$$

Considering (22) and (25), Eq. (26) can be rewritten as

$$P_d(E_{m+1}) = \frac{P_d(E_m) - \left\{\left[\frac{\sigma_s}{\epsilon_0\epsilon_f}\right] + E_m\right\}\left[\left(\frac{d}{dE}\right)P_d(E)\right]_{E_m}}{1 + \left(\frac{1}{\epsilon_0\epsilon_f}\right)\left[\left(\frac{d}{dE}\right)P_d(E)\right]_{E_m}}. \quad (27)$$

The next value of the polarization in each step can be obtained using (27). Sweeping the gate voltage and calculating the next value of the polarization in each step, the drain current is calculated as a function of the gate voltage.

The model predicted results were verified by comparing with TCAD simulation results. The device surface potential is presented in Fig. 3. First, we verified the surface potential in the middle of the channel which is the primary parameter to compute the potential profile and the drain current. The surface potential profile in the middle of the channel for different drain voltages and sweeping the gate voltage is illustrated in Fig. 3(a). Results confirm that our proposed model replicates well with the TCAD simulations. The effect of the dipole polarization on the surface potential profile along the channel is presented in Fig. 3(b). The surface potential profile is calculated for a TFET with 1 V gate voltage and 1.5 V drain voltage considering the gate oxide performs no ferroelectricity, ferroelectric with $-0.3\ \mu C/cm^2$, and $5\ \mu C/cm^2$ values of polarization to illuminate the effect of the positive and negative values of the polarization on the potential profile. Finally, the output current of the device is shown in Fig. 4. Fig. 4(a) represents the output current while the drain voltage is 1.5 V. The device's transfer

characteristic for 1.5 V drain voltage and different sweeps of the gate voltage is illustrated in Fig. 4(b).

3. Memory window

The memory window (MW), a critical parameter in nonvolatile memory devices, is the threshold voltage difference between the two states of the device. Here, the constant current method at $10^{-7}\ A/\mu m$ is utilized for threshold voltage extraction [27]. The memory window should be large enough to ensure a significant retention time and ease of data detection in nonvolatile memories. In this section, we discuss the quantitative influence of different device parameters that affect the memory window based on our presented model and theoretically highlight the advantages of the silicon-doped HfO$_2$ ferroelectric thin film.

3.1. Ferroelectric material

It is well known that a Fe-FET memory window while the ferroelectric layer contains a sufficient remanent polarization and having the electric field higher than the material's coercive field mostly depends on the ferroelectric coercive field and thickness. In this subsection, we investigate the effect of the ferroelectric coercive field on the Fe-TFET memory window using the same thickness of different ferroelectrics. The properties of two well-known perovskite ferroelectrics, Lead Zirconate Titanate (PZT) and Strontium Barium Titanate (SBT), is compared with Si:HfO$_2$ in Table 1. The recently discovered ferroelectric thin film, Si:HfO$_2$ [28,6], has a relatively high coercive field that ensures a large memory window [29–39].

The $I_d - V_g$ characteristics of a Fe-TFET using 10 nm of PZT, SBT, and Si:HfO$_2$ are depicted in Fig. 5(a). We have used the same thickness of each material to eliminate the influence of the ferroelectric thickness on the MW. The Fe-TFET that is using PZT or SBT as the gate ferroelectric provides higher current level due to their higher relative permittivity comparing Si:HfO$_2$. The high dielectric constant of PZT and SBT reduces the voltage drop across the ferroelectric layer and enhances the silicon surface potential. Therefore, considering (11)–(14), the tunneling width at the source and drain tunneling junctions increases which lead to the improved tunneling current.

Based on the presented results in Fig. 5(a), Si:HfO$_2$ theoretically provides larger memory window compared to the well-known ferroelectric materials PZT and SBT. Up to 1.7 V memory window is obtained for a device using 10 nm of Si:HfO$_2$. In Fig. 5(b) different thicknesses of PZT and SBT are used to maintain the same memory window as the Fe-TFET using 10 nm of Si:HfO$_2$. 50 nm of PZT and 230 nm of SBT is required to provide 1.7 V memory window while 10 nm of silicon-doped HfO$_2$ grant the same memory window. The theoretical results provide a great insight into the benefits of the silicon-doped HfO$_2$ ferroelectric thin film. Besides the theoretical advantages of Si:HfO$_2$ comparing perovskite ferroelectrics, due to the high relative permittivity of the PZT and SBT (over 200), it is challenging to fabricate a device with a thin layer of perovskites ferroelectrics. Moreover, CMOS compatibility, scalability and the ability to deposit a high-quality layer by Atomic Layer Deposition (ALD) are some of the technological advantages of using Si:HfO$_2$.

The presented MWs in Fig. 5 are lower than the theoretical maximum of the ferroelectric field effect devices memory window ($\sim 2E_c \times d$ which is 2.2 V in the case of 10 nm Si:HfO$_2$) due to the depolarization field and gate leakage current effects. The depolarization field always exists in a ferroelectric capacitor due to the finite dielectric constant of the semiconductor that causes incomplete charge compensation. Moreover, the injected electrons from
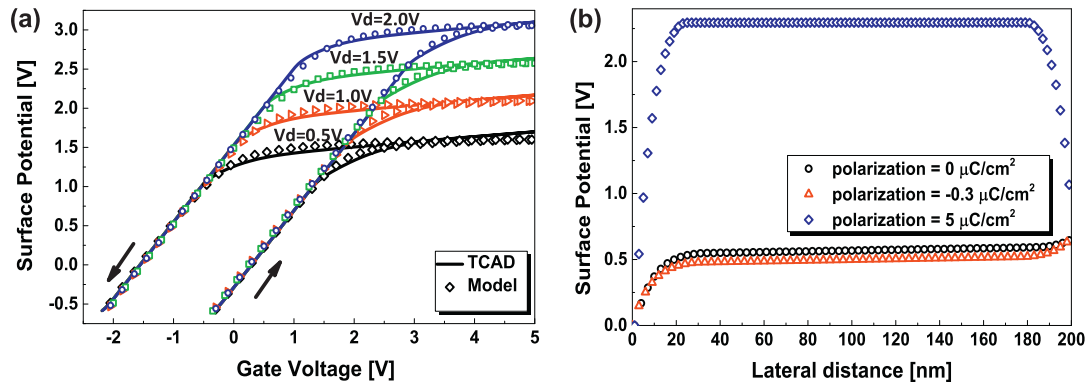
Fig. 3. Ferroelectric TFET surface potential. (a) The model verification of the surface potential in the middle of the channel using different drain voltages and sweeping the gate voltage with Sentaurus TCAD simulations results. (b) The surface potential profile along the channel with the polarization as a parameter. Results are obtained using the proposed model for a device with $V_G = 1\,V$, $V_D = 1.5\,V$, and considering the gate oxide has 0, -0.3, and 5 $\mu C/cm^2$ polarization to illustrate how the positive and negative values of the polarization affect the potential profile.
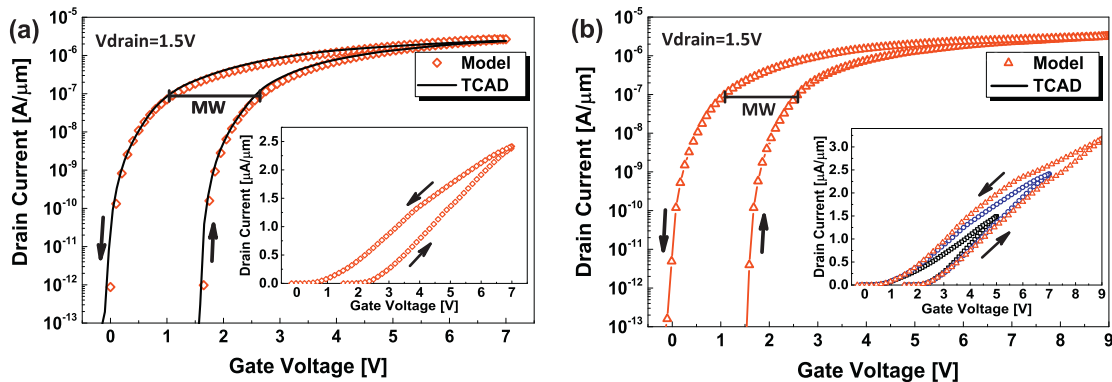

Fig. 4. The ferroelectric TFET transfer characteristic for different drain and gate voltages. (a) The Fe-TFET model vs. TCAD results obtained for 1.5 V drain voltage. (b) Fe-TFET drain current for different sweeps of the gate voltage.

Table 1
The ferroelectric properties of PZT [29–32], SBT [33–39], and Si:HfO$_2$ [28].

Ferro material	$P_r \left(\frac{\mu C}{cm^2}\right)$	$P_s \left(\frac{\mu C}{cm^2}\right)$	$E_c \left(\frac{MV}{cm}\right)$	ϵ_r
PZT	32	40	0.26	250
SBT	8	15	0.08	250
Si:HfO$_2$	9	9.5	1.1	32

the gate and semiconductor to the ferroelectric layer lead to the local charge compensation and reducing polarization [40].

3.2. Buffer layer

Due to the large number of defects, leakage current, and large lattice mismatch between perovskite ferroelectrics and silicon, it is always necessary to use a buffer layer with a proper interface
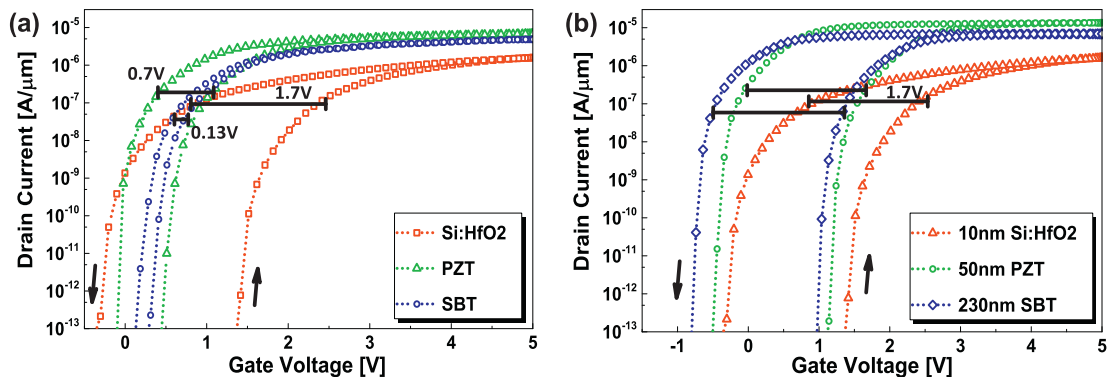

Fig. 5. (a) The transfer characteristic of Fe-TFETs using 10 nm of PZT, SBT, and Si:HfO$_2$ as the gate ferroelectric obtained by our proposed model. The device benefits from doped HfO$_2$ thin film provides larger memory window due to its high coercive field while all ferroelectrics has the same thickness. (b) The transfer characteristic of FeTFETs using different thicknesses of mentioned ferroelectric materials providing the same memory window. 10 nm of Si:HfO$_2$, 50 nm of PZT, and 230 nm of SBT are required to provide 1.7 V memory window.

with the substrate. However, the voltage drop over the buffer layer reduces the memory window.

To study the effect of the buffer layer on the MW, we utilized 10 nm of Si:HfO$_2$ as the ferroelectric dielectric and 1 nm of SiO$_2$ and Si$_3$N$_4$ as the buffer layer. Results are compared with a device using only 10 nm of Si:HfO$_2$ as the gate stack in Fig. 6. Employing 1 nm of SiO$_2$ drops the MW to 1.0 V while the use of 1 nm of Si$_3$N$_4$ reduces the memory window to 1.2 V as the voltage drop over the buffer layer reduces the ferroelectric voltage (electric field). The voltage drop over the buffer layer is considerable as SiO$_2$ and Si$_3$N$_4$ have lower relative permittivity comparing to the ferroelectric layer. Reducing ferroelectric voltage results in the formation of minor polarization hysteresis loops instead of the saturation polarization loop that reduces the memory window significantly [16,13]. Moreover, the presence of the buffer layer reduces the silicon surface potential results in low energy carriers and insufficient tunneling through the source and drain tunneling barriers that lead to the deformation of the transfer characteristic and reduced saturation current. The negative influence of the buffer layer can be reduced in the case of high-K materials that lowers the voltage drop across this layer, but it can never be zero. In this subsection, we emphasize on another advantage of Si:HfO$_2$ which is its proper interface with silicon. Therefore, the doped HfO$_2$ thin film can be deposited directly on the silicon, and no buffer layer is required. However, it should be noted that a thin layer of HfSiO forms at the interface during the deposition and annealing of the Si:HfO$_2$ which is called the dead layer. The dead layer performs no ferroelectricity, and it behaves like a buffer layer causing reduced memory window [6,28]. As the dead layer is a related issue for all ferroelectric materials we have neglected this effect in our simulations.

Besides reducing the memory window, presence of the buffer layer also increases the subthreshold slope affecting the response time and power dissipation.

3.3. Ferroelectric thickness

Another important parameter that greatly affects the memory window is the ferroelectric thickness. The ferroelectric thickness strongly affects the MW as it specifies the total number of the dipoles ($MW \sim 2E_c \times d$ where E_c and d are the ferroelectric coercive field and thickness relatively [40]). Furthermore, the ferroelectric coercive field might change by varying the film thickness,
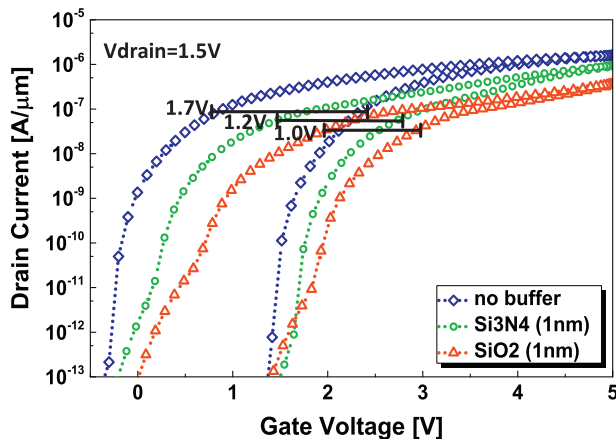
Fig. 6. The output characteristic of a Fe-TFET using 10 nm of Si:HfO$_2$ as the gate stack with devices using 10 nm of Si:HfO$_2$ and 1 nm of SiO$_2$ and Si$_3$N$_4$ as the buffer layer. The device without buffer layer provides 1.7 V memory window, 1 nm of Si$_3$N$_4$ reduces the MW down to 1.2 V, and 1 nm of SiO$_2$ provides 1.0 V memory window. The presented results are derived by employing the proposed model.

Table 2
The ferroelectric properties of Si:HfO$_2$ regarding the FIMS thickness [6,28].

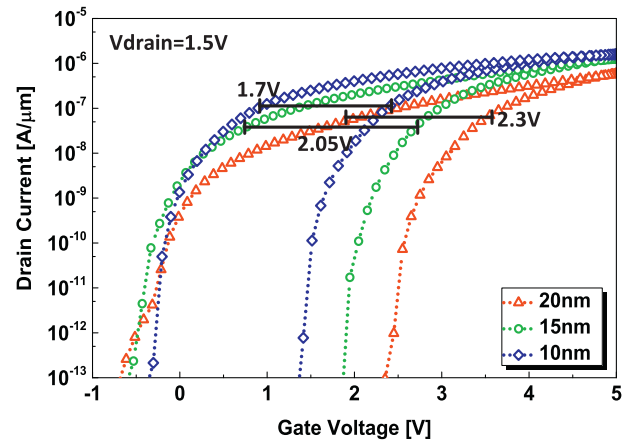| Thickness (nm)	$P_r \left(\frac{\mu C}{cm^2} \right)$	$P_s \left(\frac{\mu C}{cm^2} \right)$	$E_c \left(\frac{MV}{cm} \right)$	ϵ_r
20	5.5	5.75	1.00	28.5
15	7.25	7.62	1.05	30.25
10	9	9.5	1.1	32

Fig. 7. The $I_d - V_g$ curves of the Fe-TFETs using different thicknesses of Si:HfO$_2$. Results are obtained using our proposed model.

especially in the case of the doped HfO$_2$. Increasing the films thickness in Si:HfO$_2$ reduces the coercive field. The ferroelectric properties of the Si:HfO$_2$ regarding the film thickness is depicted in Table 2.

The transfer characteristic of the Fe-TFET using different thicknesses of Si:HfO$_2$ is illustrated in Fig. 7. The coercive field slightly reduces by increasing the silicon-doped HfO$_2$ thickness. However, simulation results confirm that the effect of the film thickness is dominant and the memory window enhances significantly by increasing the ferroelectric thickness. Up to 2.7 V memory window is obtained for a device benefits from a 20 nm layer thick Si:HfO$_2$.

4. Nanometer scale Fe-TFET

Unique properties of the ferroelectric Si:HfO$_2$ like relatively low dielectric constant, CMOS compatibility, good interface with the silicon [7], and relatively high remanent polarization even in a 5 nm thick, thin film [15] make it a promising candidate for the fabrication of future nonvolatile memories [28,6].

The unique properties of Si:HfO$_2$ allows us to fabricate ferroelectric MOSFETs down to the nanoscale. However, on the nanometer scale, the high power consumption per area of the chip becomes a challenging issue. To eliminate the power dissipation problem we need to design energy efficient devices with low *off*-current. Tunneling field effect transistors have been proposed as energy efficient devices due to their low *off*-current and steep *off* to *on* transition. The Fe-TFET can be a decent candidate for future nonvolatile memories due to its ability to provide a sufficient memory window with low power dissipation. As we did not consider short channel effects in our model, results of the model may not be reliable for a nanometer scale device. Therefore, Sentaurus TCAD commercial simulator is employed for design and simulation of a 28 nm gate length Fe-TFET.

In Fig. 8(a), the transfer characteristic of a 28 nm gate length single gate ferroelectric MOSFET is compared with Fe-TFET with the same dimensions. 10 nm of Si:HfO$_2$ is used as the gate
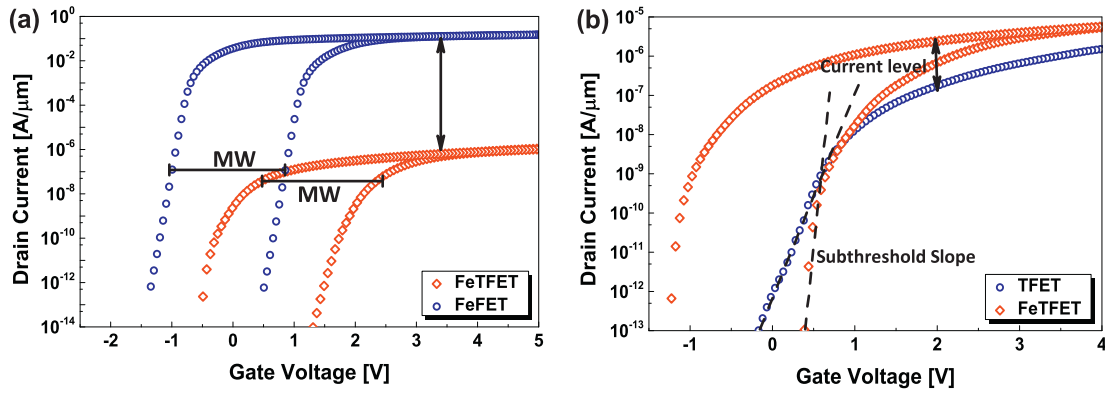
Fig. 8. (a) The transfer characteristic of a 28 nm gate length FeFET vs. Fe-TFET using 10 nm of Si:HfO$_2$ as the ferroelectric. The drain voltage is considered 1 V for all simulations which is the supply voltage of the 28 nm ITRS node. Results confirm that the Fe-TFET provides the same memory window as the FeFET with lower power consumption. (b) The negative capacitance effect enhances the output current level and subthreshold slope of the Fe-TFET comparing the conventional TFET. Results are obtained using Sentaurus TCAD commercial simulator.

ferroelectric. Regarding the presented results in Fig. 8(a), Fe-TFET provides the same memory window as FeFET with lower *off*-current (static power) and also lower *on*-current [40]. However, the TFET low output current is the main disadvantage of this device as it may not be sufficient to drive the circuit capacitors. It should be noted that besides the ability of ferroelectrics for data storage, ferroelectric transistors also benefits from the ferroelectrics negative capacitance effect that amplifies the surface potential and boosts the output current [41,42]. In Fig. 8(b), the $I_d - V_g$ characteristic of a 28 nm Fe-TFET with 10 nm of Si:HfO$_2$ is compared with a 28 nm gate length conventional TFET with the same equivalent oxide thickness. As a result of the negative capacitance effect, the subthreshold slope of the device is decreased, and the drain current is increased significantly. Simulation results illustrate that the Fe-TFET meets our expectation for a low power random access non-volatile memory providing sufficient memory window.

5. Conclusions

The analytical modeling of ferroelectric TFETs is developed and examined using Sentaurus TCAD commercial simulator. The model is obtained by solving Maxwell's first equation in conjunction with Poisson equation. Based on the proposed model, the memory window of the Fe-TFET memory devices is extensively investigated as the key parameter of nonvolatile memories. The recently discovered ferroelectric, silicon-doped HfO$_2$, is integrated into the TFET gate stack in order to highlight the advantages of this ferroelectric thin film. Theoretical results represent that Si:HfO$_2$ stands as a promising candidate for the future of ferroelectric nonvolatile memories. Besides the outstanding properties of the Si:HfO$_2$ for the device fabrication, a large memory window is obtained as the result of the integration of this ferroelectric thin film with tunneling field effect transistors. Finally, a 28 nm gate length Fe-TFET is designed and simulated providing the same MW as a 28 nm Fe-FET consuming less power dissipation. Results confirm that the Fe-TFET using Si:HfO$_2$ can be ustilized as the ultra-low power non-volatile memories. Moreover, the negative capacitance effect in ferroelectric TFETs can solve the tunneling devices main issue, low output current, by boosting the surface potential.

References

[1] Ionescu AM, Lattanzio L, Salvatore GA, De Michielis L, Boucart K, Bouvet D. The hysteretic ferroelectric tunnel FET. IEEE Trans Electron Dev 2010;57 (12):3518–24.

[2] Sakaia S, Takahashia M, Takeuchib K, Lia Q-H, Horiuchia T, Wanga S, et al. Highly scalable Fe (ferroelectric)-nand cell with MFIS (metal-ferroelectric-insulator-semiconductor) structure for sub-10 nm tera-bit capacity NAND flash memories. In: 2008 Joint non-volatile semiconductor memory workshop and international conference on memory technology and design.

[3] Müller J, Polakowski P, Müller S, Mikolajick T. Ferroelectric hafnium oxide based materials and devices: assessment of current status and future prospects. ECS J Solid State Sci Technol 2015;4(5):N30–5.

[4] Heyman P, Heilmeier G. A ferroelectric field effect device. Proc IEEE 1966;54 (6):842–8.

[5] Tokumitsu E, Nakamura R-I, Ishiwara H. Nonvolatile memory operations of metal-ferroelectric-insulator-semiconductor (MFIS) FETs using PLZT/STO/Si (100) structures. IEEE Electron Dev Lett 1997;18(4):160–2.

[6] Böscke T, Müller J, Bräuhaus D, Schröder U, Böttger U. Ferroelectricity in hafnium oxide: CMOS compatible ferroelectric field effect transistors. In: 2011 IEEE international electron devices meeting (IEDM). IEEE; 2011. p. 24–5.

[7] Mueller S, Muller J, Schroeder U, Mikolajick T. Reliability characteristics of ferroelectric thin films for memory applications. IEEE Trans Dev Mater Reliab 2013;13(1):93–7.

[8] Huang Q, Huang R, Zhan Z, Qiu Y, Jiang W, Wu C, et al. A novel Si tunnel FET with 36 mV/dec subthreshold slope based on junction depleted-modulation through striped gate configuration. In: 2012 IEEE international electron devices meeting (IEDM). IEEE; 2012 [p. 8–5].

[9] Hu C, Patel P, Bowonder A, Jeon K, Kim SH, Loh WY, et al. Prospect of tunneling green transistor for 0.1 V CMOS. IEDM Tech Dig 2010 [pp. 16–1].

[10] Ionescu AM, Riel H. Tunnel field-effect transistors as energy-efficient electronic switches. Nature 2011;479(7373):329–37.

[11] http://www.synopsys.com/tools/tcad/.

[12] Wu C, Huang R, Huang Q, Wang C, Wang J, Wang Y. An analytical surface potential model accounting for the dual-modulation effects in tunnel FETs. IEEE Trans Electron Dev 2014;61(8):2690–6.

[13] Miller S, Nasby R, Schwank J, Rodgers M, Dressendorfer P. Device modeling of ferroelectric capacitors. J Appl Phys 1990;68(12):6463–71.

[14] Zhou D, Müller J, Xu J, Knebel S, Bräuhaus D, Schröder U. Insights into electrical characteristics of silicon doped hafnium oxide ferroelectric thin films. Appl Phys Lett 2012;100(8):082905.

[15] Mueller S, Summerfelt SR, Müller J, Schroeder U, Mikolajick T. Ten-nanometer ferroelectric films for next-generation FRAM capacitors. IEEE Electron Dev Lett 2012;33(9):1300–2.

[16] Lue H-T, Wu C-J, Tseng T-Y. Device modeling of ferroelectric memory field-effect transistor (FeMFET). IEEE Trans Electron Dev 2002;49(10):1790–8.

[17] Miller S, McWhorter P. Physics of the ferroelectric nonvolatile memory field effect transistor. J Appl Phys 1992;72(12):5999–6010.

[18] Miller S, Schwank J, Nasby R, Rodgers M. Modeling ferroelectric capacitor switching with asymmetric nonperiodic input signals and arbitrary initial conditions. J Appl Phys 1991;70(5):2849–60.

[19] Kumar MJ, Janardhanan S. Doping-less tunnel field effect transistor: design and investigation. IEEE Trans Electron Dev 2013;60(10):3285–90.

[20] James S, Arujo P, Carlos A. Ferroelectric memories. Science 1989;246 (4936):1400–5.

[21] Zuleeg R, Wieder H. Effect of ferroelectric polarization on insulated-gate thin-film transistor parameters. Solid-State Electron 1966;9(6):657–61.

[22] Landau L, Khalatnikov I. On the anomalous absorption of sound near a second order phase transition point. Dokl Akad Nauk SSSR, vol. 96. p. 469–72.

[23] Lo VC. Simulation of thickness effect in thin ferroelectric films using Landau-Khalatnikov theory. J Appl Phys 2003;94(5):3353–9.

[24] Zhang W, Bhattacharya K. A computational model of ferroelectric domains. Part I: model formulation and domain switching. Acta Mater 2005;53 (1):185–98.

[25] Yan R-H, Ourmazd A, Lee KF. Scaling the Si MOSFET: from bulk to SOI to bulk. IEEE Trans Electron Dev 1992;39(7):1704–10.

[26] Kane E. Zener tunneling in semiconductors. J Phys Chem Solids 1960;12(2):181–8.

[27] Boucart K, Ionescu AM. Threshold voltage in tunnel FETs: physical definition, extraction, scaling and impact on IC design. In: 37th European solid state device research conference, 2007, ESSDERC 2007. IEEE; 2007. p. 299–302.

[28] Mueller S, Yurchuk E, Slesazeck S, Mikolajick T, Muller J, Herrmann T, et al. Performance investigation and optimization of Si: Hfo$_2$ FeFETs on a 28 nm bulk technology. In: 2013 IEEE international symposium on the applications of ferroelectric and workshop on the piezoresponse force microscopy (ISAF/PFM). IEEE; 2013. p. 248–51.

[29] Kanno I, Fujii S, Kamada T, Takayama R. Piezoelectric properties of c-axis oriented Pb (Zr, Ti) O3 thin films. Appl Phys Lett 1997;70(11):1378–80.

[30] Grossmann M, Lohse O, Bolten D, Boettger U, Schneller T, Waser R. The interface screening model as origin of imprint in PbZr$_x$Ti$_{1-x}$O$_3$ thin films. I. Dopant, illumination, and bias dependence. J Appl Phys 2002;92(5):2680–7.

[31] Moazzami R, Hu C, Shepherd WH. Electrical characteristics of ferroelectric PZT thin films for dram applications. IEEE Trans Electron Dev 1992;39(9):2044–9.

[32] Nakamura T, Nakao Y, Kamisawa A, Takasu H. Preparation of Pb (Zr, Ti) O3 thin films on electrodes including IrO2. Appl Phys Lett 1994;65(12):1522–4.

[33] Amanuma K, Hase T, Miyasaka Y. Preparation and ferroelectric properties of SrBi$_2$Ta$_2$O$_9$ thin films. Appl Phys Lett 1995;66(2):221–3.

[34] Al-Shareef H, Dimos D, Boyle T, Warren W, Tuttle B. Qualitative model for the fatigue-free behavior of SrBi$_2$Ta$_2$O$_9$. Appl Phys Lett 1996;68(5):690–2.

[35] Zhang Z, Wang Y, Zhu J, Yan F, Lu X, Shen H, et al. Retention characteristics of SrBi$_2$Ta$_2$O$_9$ thin films prepared by metalorganic decomposition. Appl Phys Lett 1998;73(25):3674–6.

[36] Lee HN, Visinoiu A, Senz S, Harnagea C, Pignolet A, Hesse D, et al. Structural and electrical anisotropy of (001)-, (116)-, and (103)-oriented epitaxial SrBi$_2$Ta$_2$O$_9$ thin films on SrTio3 substrates grown by pulsed laser deposition and (103)-oriented epitaxial SrBi$_2$Ta$_2$O$_9$ thin films on SrTio3 substrates grown by pulsed laser deposition. J Appl Phys 2000;88(11):6658–64.

[37] Mikolajick T, Dehm C, Hartner W, Kasko I, Kastner M, Nagel N, et al. FERAM technology for high density applications. Microelectron Reliab 2001;41(7):947–50.

[38] Mört M, Schindler G, Hartner W, Kasko I, Kastner MJ, Mikolajick T, et al. Low temperature process and thin SBT films for ferroelectric memory devices. Integr Ferroelectr 2000;30(1-4):235–44.

[39] Hartner W, Schindler G, Bosk P, Gabric Z, Kastner M, Beitel G, et al. Integration of H2 barriers for ferroelectric memories based on SrBi$_2$Ta$_2$O$_9$ (SBT). Integr Ferroelectr 2000;31(1-4):273–84.

[40] Ma T, Han J-P. Why is nonvolatile ferroelectric memory field-effect transistor still elusive? IEEE Electron Dev Lett 2002;23(7):386–8.

[41] Rusu A, Salvatore GA, Jimenez D, Ionescu AM. Metal-ferroelectric-meta-oxide-semiconductor field effect transistor with sub-60mv/decade subthreshold swing and internal voltage amplification. In: 2010 IEEE international electron devices meeting (IEDM). IEEE; 2010 [p. 16–13].

[42] Salahuddin S, Datta S. Use of negative capacitance to provide voltage amplification for low power nanoscale devices. Nano letters 2008;8(2):405–10.